Distributed Massive MIMO Channel Measurements in Urban Vehicular Scenario

David Löschenbrand, Markus Hofer, Laura Bernadó, Gerhard Humer,
Bernhard Schrenk, Stefan Zelenbaba, Thomas Zemen
Security & Communication Technologies, Austrian Institute of Technology GmbH, Vienna, Austria
david.loeschenbrand@ait.ac.at

***Abstract*—We present a measurement framework for rapidly time-varying distributed massive multiple-input multiple-output (MIMO) channels. We introduce a custom-built calibration device to facilitate calibration of multiple transceivers as well as a synchronization structure for distributed massive MIMO arrays. Measurements are performed with two transmit and 32 receive antennas in parallel with 115 MHz bandwidth and 1 ms repetition rate at a carrier frequency of 3.52 GHz. The transmit antennas are mounted on a car moving through an urban environment while the receive antennas are placed on the rooftop of a building. We analyze the measured channel characteristics and the singular value spread over time for collocated and distributed receive antenna setups. Our results show that collocated receiver arrays outperform the distributed ones in terms of the singular value spread for the given scenario.**

***Index Terms*—massive MIMO, measurement, vehicular, distributed, calibration.**

I. Introduction

The wireless propagation channel fundamentally determines the performance of wireless communication systems. Vehicular scenarios pose a great challenge to communication systems due to the large (relative) velocities, many moving metallic reflectors and low flexibility in antenna placement [1]. Massive multiple-input multiple-output (MIMO) is widely considered as a key enabling technology for 5G [2]. It promises increased spectral efficiency and the mitigation of small-scale fading through channel hardening due to the large amount of base station (BS) antennas [3]. Spectral efficiency is of uttermost importance for enhanced mobile broadband (eMBB) applications. Channel hardening, however, is a key feature for ultra-reliable low latency communication (URLLC) because large fading dips causing the loss of possibly safety-critical messages can be avoided.

The utilization of massive MIMO communication links for vehicle to infrastructure (V2I) applications in safety-critical scenarios promises reliability and robustness against harsh propagation conditions found in vehicular settings. The characterization of this propagation conditions (via *channel sounding*) lays the foundation for future URLLC systems. Due to the rapidly time-varying and non-stationarity behavior of the channel, common measurement methods with switched radio frequency (RF) chains or virtual antenna arrays are not applicable to V2I scenarios.

In this work, we present a fully parallel distributed massive MIMO channel sounder suitable for characterizing 32 vehicular channels with high velocities in parallel (extendable to 96 channels). A custom-built calibration unit facilitates the calibration of the RF chains. A flexible synchronization solution allows for antenna nodes which are distributed up to $60\,\mathrm{m}$ in space.

Scientific Contribution

- First massive MIMO channel sounder for vehicular scenarios with 32 calibrated receiver chains (extendable to 96)
- Distributed antenna array with $60\,\mathrm{m}$ distance, which is extendable to $200\,\mathrm{m}$ with White Rabbit (WR)

II. Channel Acquisition and Analysis

A. Channel Sounding Principle

Vehicular wireless channels exhibit rapidly time-varying behavior and non-stationary statistics [4]. We use a sampled, complex baseband multitone signal

$$x_n = x(nT/Q) = \sum_{q=-(Q-1)/2}^{(Q-1)/2} X_q e^{i2\pi \frac{qn}{Q}} \tag{1}$$

to capture the channel characteristic over time. The sampled time signal x_n is formed by a superposition of Q tones (we assume Q to be odd) with complex weight X_q and frequency spacing $\Delta f = 1/T$. The numerous degrees of freedom in this formulation are utilized to achieve equal power of all tones (i.e. $|X_q| = 1$) and a low crest factor [5]

$$C = \frac{\max_{t\in[0,T]} |x(t)|}{\sqrt{\frac{1}{N}\int_0^T |x(t)|^2\,dt}} \tag{2}$$

of the continuous signal over the period $T = 1/\Delta f$. A low crest factor is achieved by optimizing the phases of the complex weights X_q with the algorithm proposed in [6].

The multitione signal used for the measurements in this paper features a frequency resolution of $\Delta f = 240\,\mathrm{kHz}$ and $Q = 481$ tones, thus yielding a bandwidth of $B = 115.44\,\mathrm{MHz}$, with a crest factor $C = 1.24$. The periodic multitone signal is transmitted four times to form the sounding sequence for one transmitter of length $4T \approx 16.67\,\mu\mathrm{s}$. The first repetition acts as cyclic prefix (CP), the second and third repetition constitute the signal, and the fourth repetition acts as guard period. Each additional transmitter uses a time shifted

version of this sounding sequence to avoid overlap in time due to multipath.

On the receiver, the sounding sequence y_n including CP and additional guard periods is sampled and stored. Since the sounding procedure resembles a CP orthogonal frequency-division multiplexin (OFDM) scheme, the received symbols are obtained via discrete Fourier transform, i.e. $Y_{\tilde{q}} = \mathrm{FFT}\{y_n\}$ [5]. The signal part of the sounding sequence contains two repetitions of the multitone signal (1). Therefore, every other frequency bin $Y_q = Y_{2\tilde{q}}$ constitutes the uncalibrated transfer function of the propagation channel and the radio front-ends. Fig. 1 shows the full signal structure. The transmitted symbols X_q are known at the receiver and the calibrated transfer function estimate of the channel is thus obtained by

$$\hat{H}_q = \frac{Y_q}{X_q \hat{H}_q^{\mathrm{RF}}}. \tag{3}$$

The transfer function $\hat{H}_q^{\mathrm{RF}}$ of the RF chains is obtained in a calibration step detailed in Sec. III-B.

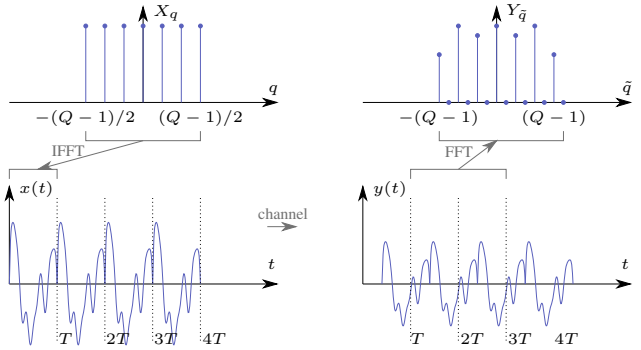

Fig. 1. Signal structure of the channel sounder. The complex tone weights X_q are transformed into time domain via IFFT. The resulting sampled time signal x_n is concatenated four times and transmitted over the radio channel. At the receiver, the whole sounding sequence is stored. A part of length $2T$ is used to obtain an oversampled estimate of the propagation channel via an FFT.

B. Characterization of Massive MIMO Channels

The notation introduced in the previous section considers one transmitter and one receiver. In the massive MIMO uplink case, the number of receive antennas M is far greater than the number of transmit antennas K, $M \gg K \geq 1$. With $\mathbf{x}_q = [X_{q,1}, \dots X_{q,K}]^T$ grouping the signals $X_{q,k}$ of the k-th transmitter into vector form (similarly, $\mathbf{y}_q = [Y_{q,1}, \dots Y_{q,M}]^T$ for the receiver), the MIMO uplink signal model reads

$$\mathbf{y}_q = \mathbf{H}_q \mathbf{x}_q + \mathbf{z}_q. \tag{4}$$

The channel matrix $\mathbf{H}_q = [\mathbf{h}_{q,1}, \dots \mathbf{h}_{q,K}]$ of dimension $M \times K$ contains the channel vectors $\mathbf{h}_{q,k}$ from transmitter k to all receivers on a given subcarrier q and the noise $\mathbf{z}_q$ is considered random complex Gaussian.

Decomposing the channel matrix

$$\mathbf{H}_q = \mathbf{U}_q \mathbf{\Sigma}_q \mathbf{V}_q^H \tag{5}$$

into unitary matrices $\mathbf{U}_q \in \mathbb{C}^{M \times M}$, $\mathbf{V}_q \in \mathbb{C}^{K \times K}$, and the rectangular matrix $\mathbf{\Sigma}_q \in \mathbb{C}^{M \times K}$ yields K singular values $\sigma_{q,k}$ on the main diagonal of $\mathbf{\Sigma}_q$. The ratio

$$\kappa_q = \frac{\max_k \sigma_{q,k}}{\min_k \sigma_{q,k}} \tag{6}$$

of largest to smallest singular value of the channel matrix is termed singular value spread (SVS) and is often referred to as a measure of *favorable propagation* in massive MIMO systems [9]. Under favorable propagation scenarios, the inner product of the instantaneous channel matrix with itself becomes close to a diagonal matrix ($\mathbf{h}_k^T \mathbf{h}_{\tilde{k}} \approx 0$, $k \neq \tilde{k}$) and thus linear precoding becomes close to optimal. SVSs close to one indicate uncorrelated channel vectors which do not lie in the same eigenspace and thus offer larger capacity.

To analyze the time-variant characteristics of vehicular channels for a given transmitter k and receiver m, we revert to the time-variant power delay profile (PDP) and the time-variant Doppler spectral density (DSD). They are obtained as marginals of the local scattering function (LSF) (see [4], [8] for more details).

III. Channel Sounder Implementation

The transmitter node of the presented massive MIMO channel sounder consists of a software-defined radio (SDR) with a frequency range of $10\,\mathrm{MHz} - 6\,\mathrm{GHz}$ (universal software radio peripheral (USRP) 2954R). The SDR feeds two transmit antennas TX1 and TX2 with two sounding sequences multiplexed in time. To increase the transmit power, external power amplifiers (PAs) are used. The SDR is controlled and configured by a host computer. Synchronization and triggering is performed via a Rubidium clock. The setup is powered by an uninterruptible power supply (UPS) which allows for more than four hours of measurement time without the need of a power outlet. The transmitter node is placed in a small van and transmit antennas as well as GPS antennas for position tracking are mounted on the roof of the van. The transmitter node is thus mobile and can be operated at various speeds and in different propagation scenarios.

The receiver features 32 receiver chains which are operated fully parallel. We group the receive chains into two nodes, each of which features 16 transceiver chains. Both nodes are connected to a host computer via $30\,\mathrm{m}$ data and synchronization cables. This allows for a distribution of the receiver nodes of up to $60\,\mathrm{m}$. The 32 parallel receiver chains are realized using 16 USRP 2953R SDRs with a frequency range of $1.2-6\,\mathrm{GHz}$. The receiver also uses a Rubidium clock for synchronization and triggering. Fig. 2 shows a block diagram of the sounder structure.

A. Transmit and Receive Antennas

Vertical monopole antennas over a finite horizontal ground plane are used on both transmitters, yielding omni-directional vertically polarized transmit signals. The $10\,\mathrm{dB}$ bandwidth was measured to be $600\,\mathrm{MHz}$ centered at $3.5\,\mathrm{GHz}$. The

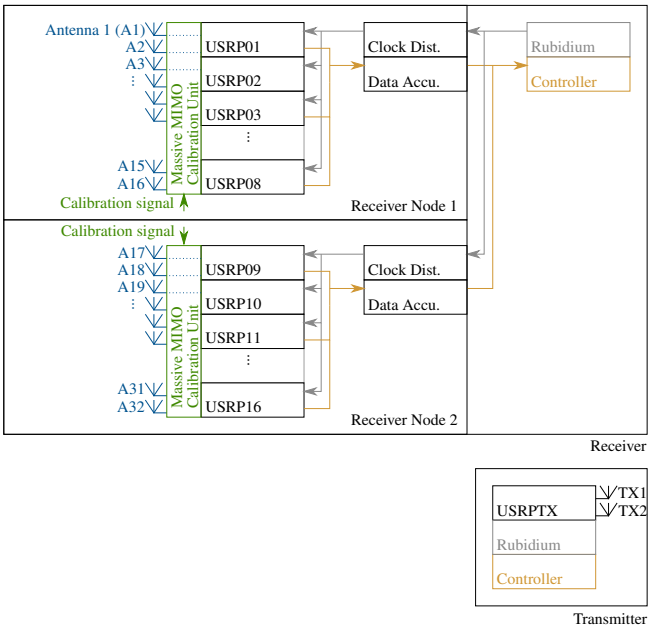

Fig. 2. Block diagram of the massive MIMO channel sounder. The receiver is divided into two nodes which can be placed arbitrarily in space with a maximum distance of 60 m. Each node consists of an antenna array (A1-A16 and A17-A32, coloured in blue). The massive MIMO calibration unit is placed between antennas and USRPs in order to facilitate calibration. The transmitter consists of one USRP connected to two antennas and supplemented with external PAs. Synchronization is provided by two Rubidium clocks (green) at transmitter and receiver, respectively.

monopole antennas are fastened to a magnetic mount to be easily deployable on the cars roof.

Air-gaped patch antenna arrays are used on both distributed receiver nodes. One array element consists of a single quadratic metallic patch with dimensions $3.05 \times 3.05\,\mathrm{cm}$ on a standard $1.52\,\mathrm{mm}$ FR4 substrate. One receiver node array consists of eight horizontal times two vertical patch elements mounted on an aluminum plate that serves as ground plane and adds mechanical stability. An air-gap of $3\,\mathrm{mm}$ is introduced between substrate and ground plane to extend the bandwidth of each patch element. The resulting array exhibits a $10\,\mathrm{dB}$ bandwidth of $250\,\mathrm{MHz}$ centered at the design frequency of $3.5\,\mathrm{GHz}$. Each patch element is connected to two antenna ports for horizontal and vertical polarization. The patch element spacing is $6\,\mathrm{cm} \approx 0.7\lambda$ in both horizontal and vertical direction. Fig. 3 depicts one RX antenna node array. The aluminum ground plane already features drill-holes for future mounting of additional patch elements.

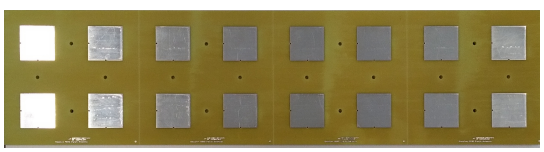

Fig. 3. RX air-gaped patch antenna array with connectors on the back for both horizontal and vertical polarization.

B. Massive MIMO Calibration Unit

A custom built massive MIMO calibration unit (see Fig. 4) is integrated in the measurement framework to ensure fast and reliable calibration of all RF chains in the system. By doing so, the non-flat frequency response of the involved converters and amplifiers is factored out. The calibration unit consists of one input port (REF) and a splitter for the calibration signal, eight antenna input ports and eight RF output ports. Externally controlled switches allow to choose if either the signals from the eight antennas or the split calibration signals are routed to the output ports. We use 4 calibration units for 32 receive chains.

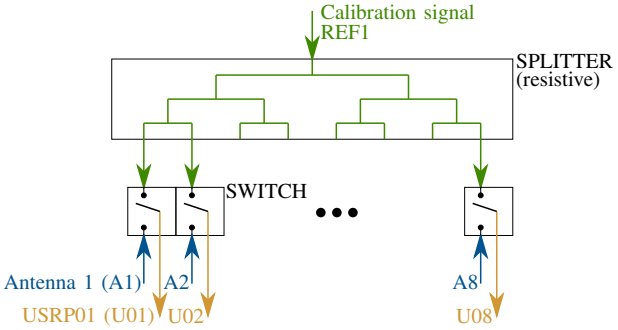

(a)

(b)

Fig. 4. Schematic (a) and fully assembled view (b) of the massive MIMO calibration unit. Externally controlled switches route either a split calibration signal (green) or the antenna signal (blue) to the RF output ports which are in turn connected to the receiver USRPs. Two units as depicted in (a) are assembled into one housing and connected to 16 RF chains as seen in (b).

The calibration procedure is the following:

1) Connect transmitter TX1 (with appropriate attenuation) to the calibration input port REF1.
2) Control the calibration unit such that the calibration signal from REF1 is fed to USRP01 - USRP04.
3) Record time samples and store for offline calibration.
4) perform steps 1) - 3) for all relevant combinations of TX1, TX2, REF1 - REF4.

Provided that the frequency response of the calibration unit is known and does not change, this procedure allows fast and reliable calibration of massive MIMO systems in the field.

C. Synchronization

a) RX-TX synchronization: A Precision Test Systems GPS10eR Rubidium clock is used on the receiver side to provide a $10\,\mathrm{MHz}$ reference signal and a 1 pulse per second

(PPS) trigger signal for timing. This Rubidium clock is used as the master clock and operated in free-run mode. An identical Rubidium clock is used to provide reference and trigger signals on the transmitter side. The transmit clock is connected via coaxial cables and disciplined to the master clock. After approximately two hours and after performing the calibration procedure, the two Rubidium clocks are separated and both operate in free-run mode. Due to the low frequency drift of the oscillator, the separated clocks can be used for synchronizing transmit and receive node.

b) RX-RX synchronization: Standard coaxial cables of $30\,\mathrm{m}$ length carry the reference and trigger signal from the synchronization source to each antenna array. This allows for a distance between fully synchronized antenna arrays of up to $\approx 60\,\mathrm{m}$. Thus, a distributed setup can easily be implemented.

An alternative synchronization method using the WR platform over fiber was investigated in [7] and found suitable to extend the antenna array distance of our channel sounder to $200\,\mathrm{m}$.

IV. Measurement Scenario and Results

Measurements are performed in an urban environment in Vienna, Austria. The two transmit antennas are placed on a small vans roof with a spacing of $1\,\mathrm{m}$. Additionally, two GPS antennas are mounted on the roof of the car and connected to the Rubidium clock to enable precise and redundant localization while moving. Inside the small van, the controller, Rubidium clock, SDR and the PAs are fixed in a 19-inch rack and powered by a UPS. The receiver is placed on the roof of a four stories high building on the premises of AIT. The two receiver nodes with 16 antennas each are either *distributed* ($7.5\,\mathrm{m}$ distance) or *collocated* ($0.5\,\mathrm{m}$ distance). Both receiver arrays face in the same direction. On both transmitter and receiver, vertically polarized antennas are used. Table I lists parameters used in the measurement.

TABLE I
Measurement parameters and their respective values.

Parameter	Value
carrier frequency f_c	$3.52\,\mathrm{GHz}$
number of tones Q	481
tone spacing Δf	$240\,\mathrm{kHz}$
bandwidth B	$115.44\,\mathrm{MHz}$
repetition rate	$1\,\mathrm{ms}$
max. Doppler frequency (velocity)	$500\,\mathrm{Hz}$, $(42\,\mathrm{m\,s^{-1}})$
TX1 (TX2) power	$25\,\mathrm{dBm}$, $(20\,\mathrm{dBm})$
measurement time per run	$90\,\mathrm{s}$
runs per scenario	10
RX node distance	$7.5\,\mathrm{m}$ (dist.), $0.5\,\mathrm{m}$ (coll.),

A. Scenario

A route around the AIT office building is selected for measurements. One measurement on this route takes $90\,\mathrm{s}$. We repeatedly run the transmitter on the defined route with a reproducible velocity profile and perform measurements. This way we generate multiple realizations of the same scenario to gain statistical significance.

In what follows, we will focus on the $20\,\mathrm{s} - 40\,\mathrm{s}$ segment of one measurement run. The scenario under consideration in this section is the approaching of a crossing. The distance from the receiving nodes to the crossing is $285\,\mathrm{m}$. The transmitter starts close to the receiver and moves away, approaching the crossing with $\approx 10\,\mathrm{m\,s^{-1}}$, and then slows down to make a right turn.

B. Results

Fig. 5 shows the exemplary PDP (Fig. 5a) and DSD (Fig. 5b) evaluated using a multi-taper LSF [4], [8] for one transmit and one receive antenna. Due to the large bandwidth, the single delay components from various scattering sources are clearly visible in the PDP. The line of sight (LOS) is interrupted by trees next to the street. This causes large-scale power variations of the main component of more than $10\,\mathrm{dB}$. The strongest component in the DSD is caused by the transmitter driving away from the receiver and approaching the crossing with $\approx 10\,\mathrm{m\,s^{-1}}$, causing a Doppler shift of $\approx 120\,\mathrm{Hz}$. Multiple scattering objects are passed by the transmitter, causing traces from positive to negative Doppler. Deceleration of the transmitter before turning right on the crossing causes smaller Doppler shifts of the main component and all the scattering components at the end of the shown segment.

Fig. 6 shows the SVS for the measured channel matrix both in the distributed ($7.5\,\mathrm{m}$ receiver node distance) and the collocated ($0.5\,\mathrm{m}$ receiver node distance) case. Fig. 6a (distributed case) exhibits three distinct spikes at the exact times when there is a LOS connection (also refer to Fig. 5). Surprisingly, the collocated case in Fig. 6b does not exhibit the same spikes and shows a lower SVS in general.

Considering subsets of the measured channel matrices and performing a statistical evaluation over multiple measurement runs offers the possibility to evaluate the empirical probability distribution of the SVS for a varying number of receive antennas, see Fig. 7. The higher the receive antenna count, the lower the SVS on average and the lower the probability for highly correlated channel vectors. Interestingly, the collocated receiver setup again seems to outperform the distributed case. For the case of 16 receive antennas, they are chosen to be arranged horizontally, i.e. using only the lower row of antenna array elements on both receiver nodes (see Fig. 3). Adding another 16 antennas on top (i.e. the upper row of antenna array elements) does not improve the SVS performance. This hints at low angular diversity in the elevation domain.

V. Conclusion

We presented a measurement framework for characterizing time-variant non-stationary wireless massive MIMO radio channels. We introduced a calibration unit to facilitate accurate calibration of the channel sounders RF chains. The operation of the sounder was demonstrated with collocated and distributed receiver nodes. The large bandwidth and high

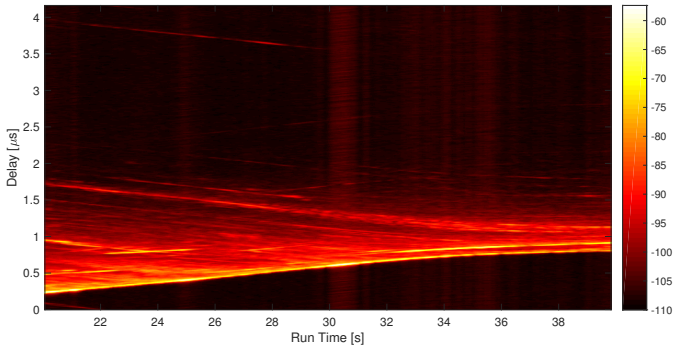

(a)

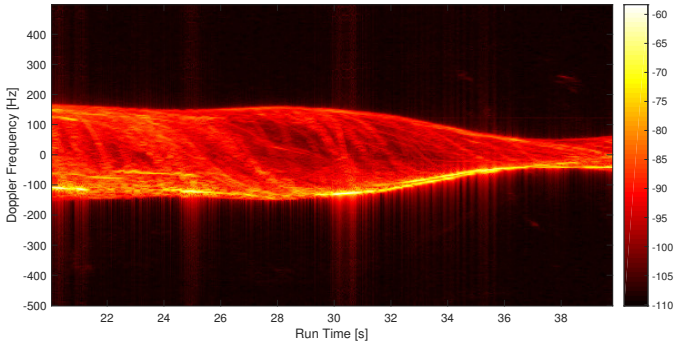

(b)

Fig. 5. PDP (a) and DSD (b) of one measured channel for a duration of 20 s. The PDP shows a rich scattering environment with a strong LOS path, a second strong path with a delay of 120 ns from 32 s − 40 s and various additional multipath components. The DSD shows a strong component with increasing negative Doppler shift. The transmitter is moving away from the receiver, approaching a crossing with $\approx 40\,\mathrm{km\,h^{-1}}$ and decelerating before turning right.

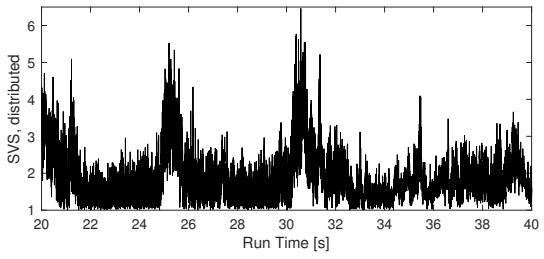

(a)

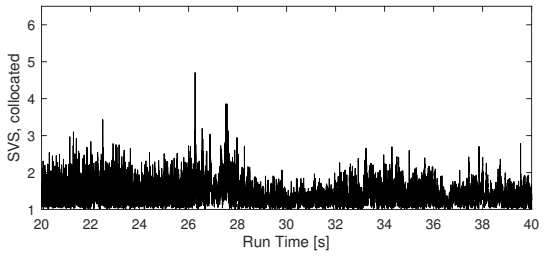

(b)

Fig. 6. SVS for one run with the receiver nodes distributed (a) and collocated (b). The three spikes in the distributed case coincide with the three LOS regions in Fig. 5. The collocated receiver setup does not show this behavior.

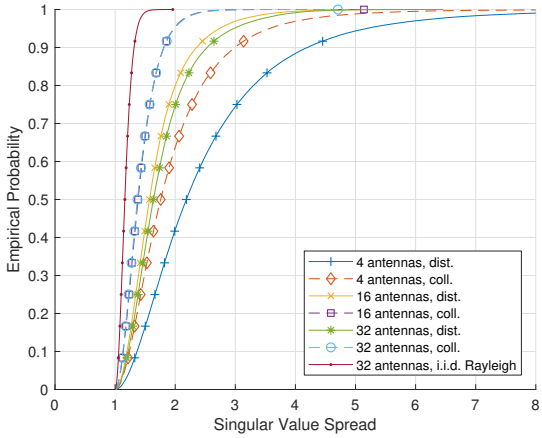

Fig. 7. Empirical CDF of the SVS over 10 runs with the distributed setup and 10 runs with the collocated setup. A subset of the measured 32×2 channel matrix with size 4×2 and 16×2 is used to simulate less receiver antennas.

repetition rate of the sounder allowed detailed analysis of the radio channels PDP and DSD. The SVSs of the obtained channel matrices were investigated and in average showed lower values for collocated receiver nodes.

Acknowledgment

This work has been performed under the framework of COST Action CA15104, Inclusive Radio Communication Networks for 5G and beyond (IRACON).

References

[1] C. F. Mecklenbräuker, A. F. Molisch, J. Karedal, F. Tufvesson, A. Paier, L. Bernadó, T. Zemen, O. Klemp, and N. Czink, "Vehicular channel characterization and its implications for wireless system design and performance," *Proceedings of the IEEE*, vol. 99, no. 7, pp. 1189–1212, 2011.

[2] L. Lu, G. Y. Li, A. L. Swindlehurst, A. Ashikhmin, and R. Zhang, "An overview of massive MIMO: Benefits and challenges," *IEEE Journal on Selected Topics in Signal Processing*, vol. 8, no. 5, pp. 742–758, 2014.

[3] T. L. Marzetta, "Noncooperative cellular wireless with unlimited numbers of base station antennas," *IEEE Transactions on Wireless Communications*, vol. 9, no. 11, pp. 3590–3600, 2010.

[4] L. Bernadó, T. Zemen, F. Tufvesson, A. F. Molisch, and C. F. Mecklenbräuker, "Delay and Doppler Spreads of Non-Stationary Vehicular Channels for Safety Relevant Scenarios," *IEEE Transactions on Vehicular Technology*, vol. 63, no. 1, pp. 82–93, 2014. [Online]. Available: http://arxiv.org/abs/1305.3376

[5] A. F. Molisch, *Wireless Communications*. John Wiley & Sons, 2011.

[6] M. Friese, "Multitone signals with low crest factor," *IEEE Transactions on Communications*, vol. 45, no. 10, pp. 1338–1344, 1997.

[7] T. Bigler, A. Treytl, D. Löschenbrand, and T. Zemen, "High Accuracy Synchronization for Distributed Massive MIMO using White Rabbit," in *2018 IEEE International Symposium on Precision Clock Synchronization for Measurement, Control, and Communication (ISPCS)*, 2018.

[8] G. Matz, "On non-WSSUS wireless fading channels," *IEEE Transactions on Wireless Communications*, vol. 4, no. 5, pp. 2465–2478, 2005.

[9] H. Q. Ngo, E. G. Larsson, and T. L. Marzetta, "Aspects of favorable propagation in Massive MIMO," *European Signal Processing Conference*, no. 1, pp. 76–80, 2014.